Title
A computationally engineered RAS rheostat reveals RAS–ERK signaling dynamics

Journal
Nature Chemical Biology, 13(1)

ISSN
1552-4450

Authors
Rose, John C
Huang, Po-Ssu
Camp, Nathan D
et al.

Publication Date
2017

DOI
10.1038/nchembio.2244

Peer reviewed

HHS Public Access

Author manuscript

Nat Chem Biol. Author manuscript; available in PMC 2017 May 21.

Published in final edited form as:

Nat Chem Biol. 2017 January ; 13(1): 119–126. doi:10.1038/nchembio.2244.

A computationally engineered RAS rheostat reveals RAS/ERK signaling dynamics

John C. Rose[1], **Po-Ssu Huang**[2,6,†], **Nathan D. Camp**[3], **Jordan Ye**[4], **Andrew M. Leidal**[4], **Inna Goreshnik**[2], **Bridget M. Trevillian**[1], **Miles S. Dickinson**[1], **Daniel Cunningham-Bryant**[1], **Jayanta Debnath**[4], **David Baker**[2,5,6], **Alejandro Wolf-Yadlin**[3], and **Dustin J. Maly**[1,2,*]

[1]Department of Chemistry, University of Washington, Seattle, Washington 98195 U.S.A

[2]Department of Biochemistry, University of Washington, Seattle, Washington 98195 U.S.A

[3]Department of Genome Sciences, University of Washington, Seattle, Washington 98195 U.S.A

[4]Department of Pathology and Helen Diller Family Comprehensive Cancer Center, University of California San Francisco, San Francisco, California 94143 U.S.A

[5]Institute for Protein Design, University of Washington, Seattle, Washington 98195 U.S.A

[6]Howard Hughes Medical Institute, University of Washington, Seattle, Washington 98195 U.S.A

Abstract

Synthetic protein switches controlled with user-defined inputs are powerful tools for studying and controlling dynamic cellular processes. To date, these approaches have relied primarily on intermolecular regulation. Here, we report a computationally-guided framework for engineering intramolecular regulation of protein function. We utilize this framework to develop Chemically Inducible Activator of RAS (CIAR), a single-component RAS rheostat that directly activates endogenous RAS in response to a small molecule. Using CIAR, we show that direct RAS activation elicits markedly different RAS/ERK signaling dynamics compared to growth factor stimulation, and that these dynamics differ between cell types. We also found that the clinically-approved RAF inhibitor vemurafenib potently primes cells to respond to direct wild-type RAS activation. These results demonstrate the utility of CIAR for quantitatively interrogating RAS signaling. Finally, we demonstrate the general utility of our approach to design intramolecularly-regulated protein tools by applying this methodology to the Rho Family GEFs.

*Correspondence: maly@chem.washington.edu (Tel: 206-543-1653/ FAX: 206-685-7002).
†Current address: Department of Bioengineering, Stanford University, Stanford, California 94305, U.S.A.

Author Contributions

J.C.R. and D.J.M. conceived the project and designed the study. J.C.R. and P-S.H. developed computational methods and performed the design calculations with guidance from D.B. J.C.R., I.G, and D.C.B. performed biochemical experiments. J.C.R, J.Y., and M.S.D. performed cell biology experiments under the supervision of J.D. and D.J.M. J.C.R, A.M.L., M.S.D., and B.M.T. generated reagents and cell lines. J.C.R. generated samples for mass spectrometry experiments. N.D.C. prepared peptide samples, performed MS analyses, and processed MS data under the supervision of A.W-Y. J.C.R., D.J.M., N.D.C., and A.W-Y analyzed the MS data. J.C.R., P-S.H., and D.J.M. wrote the manuscript. All authors read and approved the manuscript.

Competing financial interests

The authors declare no competing financial interests.

Introduction

Engineered regulatory systems have emerged as useful tools for both studying and manipulating dynamic cellular processes[1,2]. These methods allow temporally precise control of a protein of interest with a researcher-defined input. Such perturbations are ideal for interrogating signaling networks, which are dynamic and act on rapid timescales. With few exceptions[3–6], methods for chemical genetic and optogenetic activation of signaling networks have relied on multi-protein, intermolecular regulatory systems[2,7–10] that are only applicable to proteins that can be sequestered from their sites of function. Despite several advantages, intramolecular regulatory systems have been far less utilized. As only a single protein component is used, intramolecular regulatory systems can be rapidly transported to diverse cellular systems while obviating issues of stoichiometry. In addition, because intramolecularly regulated proteins do not rely on redistribution to control activity, they can be localized to a site of action in the autoinhibited state, allowing application to signaling systems independent of component location. Furthermore, basal localization to sites of function may permit more rapid responses to inputs. Finally, inter- and intramolecular systems can be integrated, allowing researchers to encode more complex responses with multiple layers of regulation. In large part, the dearth of synthetic intramolecularly regulated protein systems is due to the difficulty inherent in engineering allostery[11].

Here, we describe a computationally-guided framework for intramolecular regulatory design. This approach was applied to an activator of the RAS GTPases, which couple transmembrane receptors to intracellular signaling pathways and regulate diverse cellular processes[12]. Guided by our computational approach, we generated a genetically-encoded RAS rheostat, which we termed Chemically Inducible Activator of RAS (CIAR), capable of tunably controlling endogenous RAS activation state with high temporal precision. Using CIAR, we demonstrate that direct RAS activation drives sustained ERK phosphorylation, whereas epidermal growth factor (EGF) stimulation yields a transient response. Furthermore, direct activation of RAS elicits distinct phosphorylation kinetics in the RAS/ERK module in two different cell lines. CIAR was used with genetic/pharmacological perturbations and global phosphoproteomics to provide insight into the kinetics of RAS-driven signaling cascades. Finally, we demonstrate the generality of our computational approach in guiding the design of intramolecularly-regulated systems through application to Rho Family GEFs.

Results

Computational design of an autoinhibited RAS activator

In developing a RAS rheostat, we integrated a synthetic regulatory switch with the RAS activator Son of sevenless (SOS)—a RAS guanine nucleotide exchange factor (Fig. 1a). SOS can be minimized to a constitutively-active catalytic unit (SOScat), consisting only of the Cdc25 and Rem domains[13], which we predicted could be autoinhibited by constraining a protein-protein interaction complex over the active site (Fig. 1b). We selected the interaction between BCL-xL and BH3 peptides as a synthetic regulatory switch because cell-permeable, small-molecule disruptors of this well-characterized protein-protein interaction, including A-385358 (“A3”)[6,14], are available. Critical for computational design, the BH3 peptide

("BH3") and BCL-xL complex forms a rigid body that can be modeled as a single protein domain.

For synthetic regulatory system design, one of the most critical parameters was the selection of linkers connecting BH3 and BCL-xL to SOScat's termini. Optimal linkers must satisfy three Design Criteria: (1) be of sufficient length to allow intramolecular BH3/BCL-xL complex formation; (2) the energetic local minimum for this complex must reside over SOScat's active site; and (3) the energetic landscape surrounding this minimum must be sufficiently steep-walled to ensure active site occlusion. Because potential permutations of N- and C-terminal linker lengths—"linker-space"—are too expansive to screen experimentally, *RosettaRemodel* was employed[15]. To simplify simulations and avoid exhaustive sampling, the BH3/BCL-xL complex was treated as a rigid body within a loop that bridges SOScat's termini. Modeling is, thus, reduced to a loop closure problem based on linker geometry, and the simulated low-energy ensemble–representing all the viable solutions that allow the loop to connect on both ends without strain–is assumed to correlate with the localization of the BH3/BCL-xl complex. To quantitate the localization parameter, we defined a metric, μ, as the distance between the center-of-mass (CoM) of RAS bound to the active site of SOScat and the CoM of the BH3/BCL-xL complex in each output model (Fig. 1c). μ serves as a metric for guiding empirical screening by measuring the deviation of the BH3/BCL-xL complex from SOScat's active site.

Preliminary modeling suggested that BH3 be placed at the N-terminus of SOScat and BCL-xL at the C-terminus. For each trajectory, an arbitrary break in the linkers was introduced, and subsequent chain closure only occurred in geometrically allowed models. Models without successful loop closure were discarded. Following chain closure, torsional angles within the linkers were allowed to vary in order to sample the conformations of the BH3/BCL-xL complex relative to SOScat. To gain insight into the effects of linker lengths on BH3/BCL-xL complex localization, we performed 1,000 independent sampling runs for all permutations of N- and C-terminal linkers of length {0, 5, 10, 15, 20, 25, 30} residues. The 49,000 trajectories produced 18,473 geometrically allowed models, for an overall closure rate of 37.7% (Design Criterion 1; Supplementary Results, Supplementary Fig. 1).

Next, the localization of the complex relative to SOScat's active site was evaluated. The ensemble average μ reports on the BH3/BCL-xL complex localization from SOScat's active site (Design Criterion 2). Plot of the average μ for each permutation indicates that linker length has a pronounced impact on the proximity of the BH3/BCL-xL complex to the active site (Fig. 2a). The lowest average μ (11.79 A) resulted from N-terminal linker (NL) = 15 residues and C-terminal linker (CL) = 5 residues (termed S.15.5).

Our design strategy relies on localizing the BH3/BCL-xL complex over SOScat's active site to obtain autoinhibition. Therefore, we predicted that shorter linkers would provide better autoinhibition than longer linkers by tightly constraining the BH3/BCL-xL complex over the region of RAS binding (Design Criterion 3). To estimate the mobility of the BH3/BCL-xL complex–which is a proxy for the steepness of the gradient surrounding the energetic minimum–the standard deviation (SD) of μ was calculated. As expected, shorter linker pairs yielded smaller SDs, with S.15.5 exhibiting the second smallest SD (2.53 A) (Fig. 2b).

Indeed, visualizing the BH3/BCL-xL CoM for each trajectory reveals that models of the BH3/BCL-xL complex cluster tightly over SOScat's active site for S.15.5, but are widely dispersed for longer linkers (Fig. 2c–d, Supplementary Fig. 2); suggesting that the linker space centered around (NL = 15, CL = 5) would be a promising starting point for our experimental efforts.

Biochemical and cellular refinement of CIAR design

To sample the optimal region of linker space identified through our computational approach, three candidate CIAR constructs–S.21.6, S.17.6, and S.15.3–were tested in an *in vitro* nucleotide exchange assay. All three constructs demonstrated a dose-dependent increase in RAS GEF activity in the presence of a BH3 peptide competitor, with minimal activation in the presence of a control BH3 peptide (Fig. 3a, Supplementary Fig. 3). Thus, disruption of the BH3/BCL-xL complex in *trans* leads to *in vitro* RAS activation.

A luciferase-based serum response element reporter assay for RAS/ERK pathway activation was next used to evaluate constructs in cells. We screened constructs within the linker space supported by the preceding *in vitro* exchange assay results, and found that S.17.3 exhibited the most optimal behavior. In the absence of drug, S.17.3 is highly autoinhibited (Supplementary Fig. 4), but 25 μM A3 leads to an 11.3-fold induction of luciferase reporter signal (Fig. 3b). We hypothesized that constructs containing other linkers were less optimal due to lower levels of autoinhibition for one of two reasons: (1) long linkers permit excessive conformational freedom, allowing the intact BH3/BCL-xL complex to vacate SOScat's active site or (2) short linkers disfavor the intramolecular association between BH3 and BCL-xL. Indeed, constructs with longer or shorter linkers than S.17.3 display higher levels of basal RAS activation (Supplementary Fig. 4). Together, the low basal activity, coupled with robust RAS activation upon A3 treatment, makes S.17.3 an effective Chemically Inducible Activator of RAS (from here forward referred to as CIAR).

CIAR functions as a cellular RAS rheostat

Flp-In T-REx 293 cells stably expressing either CIAR or xCIAR–a construct containing a single inactivating mutation (F929A) within SOScat[16]–(CIAR-293s and xCIAR-293s) were generated to precisely characterize CIAR's cellular behavior. Comparison of CIAR-293s and xCIAR-293s allows differentiation between direct RAS activation from potential A3 off-target effects. CIAR-293s or xCIAR-293s were treated for 30 min with A3, EGF, or DMSO to determine the effect of direct RAS activation on RAS/ERK signaling. Consistent with effective CIAR autoinhibition, similar ERK phosphorylation was observed in untreated xCIAR-293s and CIAR-293s (Fig. 3c). Provision of A3 resulted in a dose-dependent increase in phospho-ERK in CIAR-293s but no increase in xCIAR-293s, indicating that CIAR functions as a rheostat for RAS activation.

To characterize the temporal features of RAS/ERK signaling in response to direct RAS activation, an A3 and EGF treatment timecourse in CIAR-293s was performed. Consistent with previous studies[17–19], EGF elicited pronounced yet transient ERK phosphorylation. In contrast, direct RAS activation with CIAR led to a linear increase in phospho-ERK for 90 min, reaching a plateau that was sustained until at least 150 min (Fig. 3d). Phospho-ERK

levels remain elevated 48 hours post-A3 treatment in an extended timecourse (Supplementary Fig. 5). To investigate the effects of direct RAS activation in another cellular context, we generated MCF10A cells–non-transformed mammary epithelial cells–stably expressing CIAR (CIAR-MCF10As). Interestingly, similar to EGF stimulation, phospho-ERK rapidly reached a transient maximum in response to direct RAS activation, (Fig. 3e, Supplementary Fig. 6)[19]. However, unlike EGF, direct RAS activation in CIAR-MCF10As resulted in elevated ERK phosphorylation for at least 6 hours. These results indicate that ERK phosphorylation dynamics are not simply a function of RAS activation but are influenced by other factors downstream of EGFR, and by the basal wiring of the RAS/ERK module in different cell types.

Interrogation of intrinsic and extrinsic RAF regulation

We have demonstrated that direct RAS activation and EGF stimulation lead to markedly different RAS/ERK signaling module behavior in CIAR-293s. To investigate whether this is due to delayed formation of RAS•GTP, RAS activation was determined using Ras Binding Domain pull-downs (Fig. 4a). A3 treatment yielded a rapid increase in RAS•GTP in CIAR-293s, with near maximal levels within 10 min. These results suggest that, in addition to activating RAS, EGF stimulation modulates other downstream components that affect flux through the RAS/ERK module. RAF kinases—immediately downstream of RAS—are regulated by various mechanisms, including crosstalk with other signaling pathways. In particular, phosphorylation of several residues by kinases within (intrinsic) and outside (extrinsic) of the RAS/ERK signaling module have been implicated in the regulation of RAF. RAF phosphorylation dynamics were determined by profiling three RAF phosphosites —S29 and S259 in RAF1, and S365 in BRAF—using Parallel Reaction Monitoring Mass Spectrometry (PRM-MS) (Fig 4b). RAF1 S29 phosphorylation by ERK has been shown to be an intrinsic negative feedback loop of RAS/ERK signaling[20]. Inhibitory phosphorylation of RAF1 S259 and a similar site in BRAF–S365–by AKT and other kinases extrinsically regulate the RAS/ERK module[21,22]. PRM-MS revealed that RAF1 S29 phosphorylation and BRAF S365 dephosphorylation kinetics mirror that of phospho-ERK for EGF stimulation and direct RAS activation. In contrast, RAF1 phospho-S259 remained stable in response to both stimuli. Due to the absence of a response at RAF1 S259, we next profiled the status of the PI3K/AKT pathway, which is an extrinsic regulator of the RAS/ERK module, by monitoring phospho-AKT levels. Absent stimuli, AKT was phosphorylated in CIAR-293s and control T-REx 293s, and phosphorylation levels were unaffected by EGF or A3 treatment (Fig. 4c, Supplementary Fig. 7–8). Basally activated AKT in these cells could contribute to slower RAS/ERK kinetics through suppression of RAF1 activation. The divergent behavior of the extrinsic regulatory sites on RAF1 and BRAF, and the reported differential contributions of these isoforms in various cell lines[23–25], prompted further investigation of RAF regulation in CIAR-293s.

RAF recruitment to the plasma membrane, which is promoted by dephosphorylation of RAF1 S259 and BRAF S365, is critical in the regulation of the RAS/ERK module[26,27]. To examine this regulatory step, CIAR-293s were transfected with BRAF and RAF1 constitutively targeted to the plasma membrane (myrBRAF and myrRAF1). Both myrBRAF and myrRAF1 yielded constitutively active RAS/ERK signaling (Supplementary Fig. 9).

Transfection with wild-type BRAF, but not RAF1, yielded constitutively active RAS/ERK signaling, consistent with the lower levels of inhibitory regulation and higher basal activity of BRAF[26,28]. In fact, wild-type RAF1 had little effect on CIAR-mediated RAS/ERK signaling, indicating the RAS/ERK module is relatively insensitive to RAF1 but not BRAF concentration in 293 cells (Supplementary Fig. 10). To interrogate the contribution of the RAF1 phosphosites profiled in Fig. 4b, CIAR-293s were transfected with wild-type RAF1, RAF1 S29A, or RAF1 S259A prior to activation of CIAR with A3 (Fig. 4d). Abrogation of RAS/ERK intrinsic negative feedback via S29A mutation had minimal effect on RAS/ERK signaling amplitude or kinetics—consistent with two non-exclusive explanations: (1) the majority of RAS/ERK flux does not pass through RAF1 in CIAR-293s, or (2) negative feedback through RAF1 S29 is a minor regulatory mechanism in this context. In contrast, S259A RAF1 led to high basal RAS/ERK signaling prior to A3 treatment, followed by a pronounced increase in RAS/ERK flux upon CIAR activation. S259 dephosphorylation has been implicated in the relief of inhibitory 14-3-3 binding[26], and these results demonstrate that RAF1 S259 is a critical regulatory node in RAS/ERK signaling—particularly in the context of high basal PI3K/AKT signaling. Consistent with these findings, mutations of RAF1 S259 and surrounding residues, but not BRAF S365, have been observed in patients with Noonan and LEOPARD syndromes[29].

The interaction of RAF with KSR, MEK, and other RAF protomers also plays a role in RAS/ERK module regulation[26,30]. To further probe RAF regulation in response to direct RAS activation, we reasoned it might be feasible to rewire this module by pharmacologically modulating these interactions. Our efforts focused on vemurafenib, a RAF inhibitor that has demonstrated anti-tumor effects in BRAF(V600E)-driven melanomas[31,32]. Despite the clinical utility of RAF inhibitors, outgrowth of cutaneous malignancies expressing oncogenic RAS has been observed[33]. Preclinical evidence indicates vemurafenib and other RAF inhibitors induce proliferation of mutant-RAS tumors via paradoxical activation of RAS/ERK signaling in wild-type BRAF cells[34,35]. We reasoned that pre-treatment with vemurafenib may rewire the RAS/ERK module to sensitize CIAR-293 cells to direct wild-type RAS activation.

To test whether vemurafenib primes the RAS/ERK module for RAS activation, we pre-treated CIAR-293s with a range of vemurafenib concentrations prior to direct RAS activation. Based on phospho-ERK levels, we found that all concentrations of vemurafenib sensitized CIAR-293s to RAS activation (Fig. 4e). This effect was most pronounced when CIAR-293s were incubated with 1 μM vemurafenib prior to treatment with either 4 or 10 μM A3. We next sought to profile the dynamics of the RAS/ERK response in the context of vemurafenib treatment. CIAR-293s were incubated with 1 μM vemurafenib or DMSO, followed by stimulation with A3. As expected, pre-treatment with vemurafenib leads to more pronounced ERK phosphorylation relative to pre-treatment with DMSO (Fig. 4f). In CIAR-293s, this effect is strongest at 20 and 30 min after treatment with 10 μM A3. In CIAR-MCF10As, vemurafenib leads to an even greater increase in RAS/ERK signaling, which is sustained until at least 360 min (Fig. 4g). The dramatic increase in ERK phosphorylation following direct RAS activation demonstrates that vemurafenib rapidly primes the RAS/ERK module for activation. Our results demonstrate that vemurafenib only

weakly stimulates ERK signaling in the absence of RAS activation, but potently primes the RAS/ERK module to respond to direct activation of endogenous, wild-type RAS.

Phosphoproteomic profiling of direct RAS activation

The preceding results demonstrate the utility of CIAR for investigating signal propagation to a single node—ERK—downstream of RAS. We predicted that the differential dynamics of ERK phosphorylation in response to direct RAS activation versus EGF stimulation may be reflected in other phosphosites. Therefore, we used quantitative phosphoproteomics to investigate signal propagation from RAS to thousands of signaling nodes— in this case, serine/threonine phosphosites. CIAR-293s were treated with DMSO, A3, or EGF. As a control, xCIAR-293s were exposed to the same conditions. After 30 min of stimulation, cells were subjected to a modified quantitative phosphoproteomic workflow (Supplementary Fig. 11a). In CIAR-293s, 78 phosphopeptides showed significant changes in abundance after A3 treatment, while 320 phosphopeptides changed significantly in response to EGF. Of these hits, 40 phosphopeptides were shared across both conditions (Fig. 5a, Supplementary Data Set 1). In xCIAR-293s, no phosphopeptides showed significant differences in abundance upon A3 treatment relative to DMSO, indicating A3 is orthogonal to the signaling systems under investigation. Further validating the orthogonality of A3, principal components analysis reveals that A3- and DMSO-treated xCIAR-293s cluster with DMSO-treated CIAR-293s. A3- and EGF-treated CIAR-293s form their own, distinct, single-member clusters, suggesting dissimilarity in response to direct RAS activation and EGF stimulation (Fig. 5b). The differences observed between direct RAS activation and EGF stimulation after 30 min can be explained by two mechanisms: (1) phosphosites exhibiting significant differences represent signaling components uniquely modulated by either direct RAS activation or EGF stimulation, or (2) these phosphosites are modulated by both stimuli but differ in dynamics—as observed with phospho-ERK (Fig 3d).

To investigate differences in phosphorylation dynamics between direct RAS activation and EGF stimulation, a phosphoproteomic timecourse in CIAR-293s was performed (Supplementary Fig. 11b). Hierarchical clustering of the 657 phosphosites quantified in all replicates at all timepoints for both EGF and A3 treatment revealed two prominent, distinct classes of responses (Fig. 5c). Representative phosphopeptides from each class were validated via PRM-MS (Supplementary Fig. 12). Class I phosphopeptides display similar dynamics to those observed for phospho-ERK (Fig. 3d, Supplementary Fig. 12a), undergoing a rapid and transient increase after EGF stimulation but a more gradual and sustained increase in response to direct RAS activation. Of the 25 phosphosites in this class, 19 (76%) either contain an ERK substrate motif ([pS/pT]P) or derive from the ERK1/2 activation loops (Supplementary Data Sets 2 & 3). Several of these targets—including STMN1, NUP50, and TPR—are validated ERK substrates[36–38], while others—including SRSF11, HNRNPC, and MARCKS—are candidate ERK substrates[39], indicating this class is largely defined by the RAS/ERK signaling module.

In contrast to Class I, the 106 phosphopeptides that comprise Class II exhibit a rapid, pronounced, and sustained decrease in abundance in response to both EGF stimulation and direct RAS activation (Supplementary Fig. 12b). Members of this class form a highly

interconnected interaction network (Supplementary Fig. 13). Intriguingly, phosphopeptides from components of the spliceosome are significantly enriched ($p = 0.0306$, Supplementary Fig. 14). This enrichment is consistent with previous studies showing that MAPKs regulate spliceosome component phosphorylation[39], and the large number of RNA-binding protein phosphosites that have been reported to decrease in abundance within 10 minutes of EGF stimulation[18]. Phosphopeptides in this class lack appreciable differences in their responses to direct RAS activation and EGF stimulation, suggesting that RAS activation alone is sufficient to drive rapid downregulation of these phosphosites. Moreover, the rapid timescale on which these sites are downregulated suggests that the behavior of this class of peptides is not dictated by the RAS/ERK module.

Extension of computational rheostat design

To demonstrate the generality of our computational approach, the computational framework developed for SOS was retrospectively applied to a chemically inducible Rho Family GEF called Intersectin (ITSN) that we previously developed empirically[6]. We found that μ-mean and μ-SD accurately predicted the *in vitro* performance of each synthetic ITSN constructed tested, in that lower μ-mean and μ-SD values correlated with higher fold activation (Fig. 6a,b, Supplementary Fig. 15). Next, we applied this framework to the design of a chemically inducible construct of the Rho Family GEF VAV. Notably, the μ-mean surface for VAV was considerably flatter than that estimated for SOScat, indicating that Rho Family GEFs are more tolerant of linker length variations in the development of intramolecular regulation (Fig. 6c). The μ-mean and μ-SD minima (Fig. 6d, Supplementary Fig. 16) suggested constucts with NL = 2 and CL ≤ 8 (V.2.2, V.2.4, V.2.8) were promising candidates. Indeed, all three constructs tested displayed inducible GEF activity *in vitro* and showed correlation between the measured fold activation and closure frequencies (Fig. 6e–f). Simulations with closure frequency <10% generally are cases with limited solutions to satisfy the bond geometries in the linkers. The observed reduction in fold activation of constructs with low closure frequencies is reflective of modeling results suggesting that shorter linkers do not readily allow intramolecular BH3/BCL-xL interaction–do not fully satisfy Design Criterion 1. These results demonstrate that our computational framework can be applied to structurally diverse target proteins.

Discussion

Synthetic intramolecular regulation was first demonstrated for N-WASP in cell-free systems[40,41]. Subsequently, empirically engineered Rho Family GEFs governed by synthetic intramolecular regulatory systems have been described[3,6,42]. Here, we report the design and development of CIAR, an intramolecularly regulated RAS rheostat. While SOScat and Rho Family GEFs have similar enzymatic activities, SOScat is larger, more complex, and structurally unrelated to the Rho Family GEFs (Supplementary Fig. 16)[43], and a synthetic intramolecular regulatory system for SOScat has not been reported to date. To accomplish this, we developed a systematic computational framework for screening potential constructs for autoinhibition that effectively narrowed our design space. To the best of our knowledge, this is the first computational method for guiding the design of intramolecular regulation. The application of our computational framework to the design of inducible Rho Family

GEFs, demonstrates that this methodology can be used to guide the engineering of intramolecular regulatory systems for topologically diverse proteins. While a single round of design and testing was sufficient for generating intramolecularly-regulated SOScat and VAV GEFs, our computational method is amenable to further optimization, including introduction of flexibility into the target protein and model refinement based upon empirical testing. Such a computational approach can guide the engineering of synthetic regulatory regimes for a wide range of structurally and functionally diverse proteins.

In this study, our regulatory system co-opts the BCL-xL/BH3 peptide interaction to gate protein activity. From an engineering perspective, this protein-protein interaction is attractive because minimized constructs of each component are available that allow the BH3/BCL-xL complex to be treated as a single rigid body. Furthermore, the affinity of the BH3 peptide for BCL-xL can be tuned, allowing optimization of interaction strength[6]. Importantly, the small molecule (A-385358) used to disrupt the BH3/BCL-xL interaction appears to have minimal effects on endogenous signaling pathways (Fig. 5a). Furthermore, A-385358 is well-tolerated in mice[14], facilitating *in vivo* applications.

Our systematic approach for engineering autoinhibited protein rheostats was applied to RAS signaling. RAS functions as a binary switch, yet it is capable of controlling diverse and often conflicting cellular processes and phenotypes[12]. Bypassing the pleiotropic effects of growth factor stimulation and the caveats inherent to RAS overexpression methods, CIAR enables elucidation of such emergent phenomena through direct activation of endogenous RAS. Chemical genetic approaches, as with any cellular perturbation, may produce artifacts that confound interpretation of results. For this reason, we generated an inactive control, xCIAR, containing a single mutation within the SOScat active site. Comparison of results obtained with CIAR to xCIAR enabled confirmation that observed phenomena were indeed due to RAS activation rather than artifacts of small molecule treatment or localization of a chimeric transgene to the plasma membrane.

We found that the dynamics of ERK phosphorylation in CIAR-293s differ substantially between direct RAS activation and EGF stimulation, and the response to direct RAS activation also differs between cell lines. Direct RAS activation in CIAR-MCF10As elicits a rapid increase in phospho-ERK, whereas, in CIAR-293s, this increase is more gradual. Importantly, direct RAS activation via CIAR had no effect on AKT phosphorylation and did not elicit feedback activation of EGFR (Fig. 4c, Supplementary Fig. 8). RAS•GTP is rapidly formed in CIAR-293s upon A3 addition (Fig. 4a), which indicates that the observed differences between EGF and direct RAS activation, as well as between cell lines, are due to factors acting on nodes downstream of RAS. Notably, RAF regulation has been implicated as a major factor governing RAS/ERK signaling dynamics. We reasoned that the ability of CIAR to divorce RAS activation state from the pleiotropic effects of growth factors would permit the interrogation of RAF regulation dynamics. By focusing our efforts on two RAF1 inhibitory phosphorylation sites, we found that disruption of a RAS/ERK extrinsic regulatory mechanism—mediated by factors not considered components of the canonical RAS/ERK module—had a dramatic impact on RAS/ERK signaling. These results demonstrate that the wiring of signaling components extrinsic to the RAS/ERK module can strongly influence RAS/ERK kinetics, even in the absence of pleiotropic signaling stimuli.

Differences in RAS/ERK extrinsic basal wiring across cell types may contribute to the great disparities in their predisposition to oncogenic RAS-mediated transformation[44]. Furthermore, our PRM-MS results suggest RAS/ERK flux is transmitted preferentially through BRAF as compared to RAF1 in CIAR-293s in response to both EGF and direct RAS activation (Fig. 4b). Based on the rate of S365 dephosphorylation, it also appears that EGF stimulation is capable of more rapidly activating BRAF than direct RAS activation in these cells. The exact mechanistic explanation for this phenomenon remains unclear, but could involve differential modulation of phosphatases, kinases, and scaffolds[30,45,46].

We next utilized CIAR to investigate how the pharmacologic modulation of RAF affects RAS signaling. Despite clinical utility in BRAF(V600E)-driven melanomas, vemurafenib promotes the proliferation of tumors harboring oncogenic RAS and wild-type BRAF. This paradoxical activation is believed to be mediated by modulation of RAF homo- and heterodimerization and interactions with KSR and MEK[34,47,48]. In CIAR-293s and CIAR-MCF10As, we demonstrate that brief incubation with vemurafenib is sufficient to prime RAS/ERK signaling. This finding confirms that the paradoxical activation of RAS/ERK signaling by vemurafenib does not require transcriptional or translational reprogramming. Furthermore, we have shown for the first time that direct activation of wild-type RAS is sufficient to drive paradoxical activation. Previously, paradoxical activation in cells has been demonstrated in the context of oncogenic mutant RAS or upon upstream receptor activation[34,49,50]. We believe CIAR will enable further elucidation of the complex phenomenon of paradoxical activation by RAF inhibitors.

A major advantage of CIAR is the ability to evaluate the propagation of signal from RAS outward through phosphorylation networks. Quantitative phosphoproteomics revealed a class of phosphosites exhibiting dynamic behavior similar to ERK phosphorylation, while another class decreased in abundance rapidly in response to both direct RAS activation and EGF stimulation. Taken together with the investigation of RAF1 regulation, the observed differences between these classes of phosphosites suggests that the RAS/ERK module is subject to greater extrinsic regulation than other RAS driven signaling processes, at least in the context of the HEK-293-derivative line used in this study. Notably, we did not identify any prominent peptide classes, which were perturbed only by direct RAS activation and not EGF, though the dynamic behaviors of some sites differed markedly between stimuli.

In summary, we report the computationally-guided development of CIAR, a RAS rheostat. We have demonstrated the utility of CIAR in interrogating the effects of growth factor stimulation, cell type, and pharmacological rewiring on RAS signaling dynamics. Moreover, our computational framework for engineering intramolecular regulation should be applicable to a wide range of signaling proteins, guiding the development of new chemical genetic and optogenetic technologies.

Online Methods

Conformational Sampling by RosettaRemodel

The BH3/BCL-xL complex (PDB ID: 2BZW) was treated as a rigid-body connection between the N- and C-termini of the SOScat model (residues 574-1020, PDB ID: 1XD2).

The setup to allow this linkage required that we create a chain break in the SOScat structure between residues *i* and *i*+1. (The position was chosen arbitrarily, away from the termini). This circular permutation scheme allowed treatment of the insertion of BH3/BCl-xL across the termini as a loop closure problem.

We used the circularly permuted residue order on SOScat to generate blueprint files for RosettaRemodel[51]. A blueprint file defines regions to rebuild in a modeling task. The functionality for fusing a structure into the other (which is turned on with the *-insert_segment_from_pdb* flag) uses “0 x I” entries, which denote extensions of the peptide chain from the insertion PDB, in the range that corresponds to the placement of the BH3/BCl-xL complex. We varied the lengths of the linkers on either side of the BH3/BCL-xL insertion with “0 x L” entries, which denote extensions for the peptide chain by randomly selecting fragments that are loops from the fragment database. We tested loop lengths between 0 and 30, at five residue increments for the loops leading into the BH3/BCl-xl complex and for the loop leading out of it; this gives 49 different length combinations. The definition for running lengths 5 and 5 on either side of the insertion is given below: (only the residues with assignments in the blueprint file are given; in the actual blueprint, all the entries listed in the brackets were present.)

[residue entries from 1 – 36]

37 E.

38 P L PIKAA P

0 x L PIKAA G

0 x L PIKAA S

0 x L PIKAA G

0 x L PIKAA T

0 x L PIKAA G

0 x I NATRO

[167 lines corresponding to BH3/BCL-xL complex]

0 x I NATRO

0 x L PIKAA G

0 x L PIKAA S

0 x L PIKAA G

0 x L PIKAA S

0 x L PIKAA G

49 D L PIKAA D

50 V.

[residue entries from 51 and on]

The flexible part of the loops were assigned the identity of repeating glycine-(serine/threonine) residues, while their backbone conformations were sampled by introducing random combinations of torsions from loop fragments. To facilitate the conformational search, a random break was made in the loop outside of the BH3/BCL-xL region to be reconnected via both random fragment moves and chain-closure algorithms guided by the Rosetta energy function; trajectories that properly reconnected the chain were considered successful. The lowest energy model from each successful trajectory was saved as a PDB file.

The flags to run the calculations are as follows:

- database [rosetta database location]
- s [circularly permuted template PDB file]
- remodel:blueprint [blueprint files]
- insert_segment_from_pdb [PDB formatted BH3/BCL-xL complex]
- num_trajectory 20
- save_top 20
- remodel:quick_and_dirty
- use_clusters false
- vall debug1000vall
- overwrite
- max_linear_chainbreak 0.2

1000 independent trajectories were sampled in 50 parallel runs that used the flags above.

Modeling of ITSN and VAV designs was performed as above using the ITSN (PDB: 1ki1) and VAV (PDB: 3BJI) structures. sITSN designs were described previously[6].

The orientation of the terminal residues in all components were considered, and residues that are not integral to domain structures were either truncated or grouped as part of the linker to be sampled. B-factors were used to inform termini identification of rigid bodies used in modeling for SOScat, ITSN, VAV, and the BH3/BCL-xL complex (Supplementary Figure 17).

Closure frequency analysis

We placed an arbitrary lower bound on the frequency of chain closure at 10%; linker length sets giving fewer closure events than the threshold would likely fail to allow BH3/BCL-xL complex formation, i.e these linkers would fail to meet Design Criterion 1. Therefore, linker length sets yielding a closure rate <10% were excluded from further computational analysis. Additionally, we speculated that those linkers exhibiting the highest closure rates would grant the complex too many degrees of freedom, resulting in poor autoinhibition (failing Design Criterion 3).

BH3/BCL-xL complex localization analysis

The metric μ was calculated for each geometrically allowed model. This was achieved via a custom pymol script (available upon request). Briefly, the SOScat, ITSN, or VAV PDB was loaded in pymol and the Center of Mass (CoM) of RAS, CDC42, or RAC1 was determined using the center_of_mass pymol script (http://www.pymolwiki.org/index.php/Center_of_mass). Each model PDB was iteratively loaded, aligned to the SOScat, ITSN, or VAV PDB, the BH3/BCL-xL CoM determined, and the distance to the RAS, CDC42, or RAC1 CoM calculated (μ).

Plasmids

For bacterial expression, a previously described BH3 peptide (APPNLWAAQRYGRELRRMSDEGEGSFK), SOScat (res 574-1020, T968L), BCL-xL (res 2-215), and intervening variable length flexible linkers consisting of glycine-(serine/threonine) repeats were subcloned into pMCSG7 containing an N-terminal hexahistidine tag. The T968L mutation yields a constitutively active SOScat[52]. Wild-type HRAS (res 1-166) was subcloned into pMCSG7 containing an N-terminal hexahistidine tag. For expression in HEK-293T and TREx-293 cells, candidate CIAR constructs were subcloned into pcDNA5/FRT/TO, incorporating the 25 C-terminal residues of HRAS for membrane targeting. A lentiviral vector was generated by subcloning GFP, a P2A ribosomal skipping sequence, and CIAR (S.17.3) into pLenti_CMV_GFP_Puro[53]. pLenti_CMV_GFP_Puro (658-5) was a gift from Eric Campeau (Addgene plasmid # 17448). CIAR constructs used in cells utilized the following BH3 peptide sequence (APPNLWAAQRYGRELRRMADEGEGSFK). The catalytic domain of Vav2 (residues 190–374, synthesized by Genscript) was cloned with BCL-xL, BH3 peptide, and linker sequences into a pDest-527 bacterial protein expression vector using GatewayR recombination cloning technology by Life Technologies Human Rac1 (residues 1-177) was amplified from the original pcDNA3-EGFP-Rac1(wt) plasmid (Addgene plasmid #12980). The construct was cloned into a pDest-527 bacterial protein expression vector using GatewayR recombination cloning technology by Life Technologies. Wild-type, myristoylated, and BRAF and RAF1 constructs, and mutant RAF1 constructs were cloned into pcDNA3.1 via Gibson Assembly Cloning (NEB). Wild-type RAF1 sequence was PCR amplified out of pBABEpuro-CRAF, a gift from Matthew Meyerson (Addgene plasmid # 51124). Plasmids generated for this study will be made available via Addgene.

Chemicals

A-385358 (A3) was synthesized according to a previous literature procedure [14] and determined to be >95% pure by by two analytical RP-HPLC methods (eluted with either water/CH3CN or water/MeOH gradient solvent systems (+0.05% TFA) over 30 min and UV detection at 220 and 254 nm) and 1H-NMR spectroscopy

Protein Expression and Purification

CIAR constructs were expressed in *E. coli* Rosetta 2(DE3) cells by inoculating 1 L LB broth containing ampicillin (100 μg/mL). Cultures were grown at 37°C to an OD_{600} of 0.5–0.8, then induced at 15°C with IPTG (250 μM) for 18 h. To purify protein, pellets were

resuspended in CIAR Resuspension Buffer (100mM HEPES, 20 mM imidazole, 500 mM NaCl, 10% glycerol, 1 mM dithiothreitol (DTT), pH 7.5) containing PMSF (100 μg/mL) then lysed by sonication and cleared by centrifugation at 4°C. Cleared lysate was purified with Promega HisLink™ resin by rotating for 30–60 min at 4°C. Resin was washed three times with CIAR Wash Buffer (CIAR Resuspension Buffer + 50mM imidazole), then eluted with 1–3mL CIAR elution Buffer (CIAR Resuspension Buffer + 600 mM imidazole). Collected fractions were dialyzed into Assay Buffer (20mM Tris, 50mM NaCl, 10mM $MgCl_2$, 1% glycerol, 1mM DTT, pH 7.0), analyzed for purity by SDS page, aliquoted, snap frozen, and stored at −80°C. HRAS was expressed in *E. coli* Rosetta 2(DE3) cells by inoculating 2 L Terrific Broth containing ampicillin (100 μg/mL). Cultures were grown to an OD_{600} of 0.4–0.8 and induced at 18°C with IPTG (250 μM) for 18 h. HRAS protein was purified as above, except wash and elutions buffers contained no glycerol and were supplemented with GDP (5 μM) and $MgCl_2$ (500 μM).

Inducible VAV constructs were expressed as *N*-terminal hexahistidine fusions in *E. coli* Rosetta 2 (DE3) cells by inoculating LB broth containing ampicillin (100 μg/mL) and chloramphenicol (34 μg/mL). Cultures were grown at 37°C to an OD_{600} of 0.6–0.8 and induced at 20°C for 3–4 h with 1 mM IPTG. To purify the protein, cell pellets were re-suspended in His6 wash buffer (50 mM HEPES, 10 mM imidazole, pH 7.5) containing PMSF (100 μg/mL), followed by sonication and centrifugation at 4°C to clear the lysate. The cleared lysate was purified using Promega HisLink™ Protein Purification resin by rotating at 4°C for 30 min. Subsequently, the resin was washed 3x and the protein eluted with His6 elution buffer (100 mM HEPES, 400 mM imidazole, pH 7.5). Collected fractions were analyzed for purity by SDS-PAGE and dialyzed into a buffer containing 20 mM Tris, 50 mM NaCl, 2 mM DTT, pH 7.5. Constructs that were >95% pure were aliquoted, snap-frozen and stored at −80°C.

RAC1 was expressed in *E. coli* Rosetta 2(DE3) cells by inoculating 1 L of Terrific Broth containing ampicillin (100 μg/mL) and chloramphenicol (34 μg/mL). Cultures were grown at 37°C to an OD_{600} of 0.6–0.8 and induced at 25°C for 4 h with 1 mM IPTG. Bacterial pellets were re-suspended in wash buffer (10 mM HEPES, 2 mM imidazole, 1.0 mM DTT, 1.0 mM $MgCl_2$, 10 μM GDP, pH 7.5) containing PMSF (100 μg/mL), followed by sonication and centrifugation at 4°C to clear the lysate. The cleared lysate was purified using Promega HisLink™ Protein Purification resin by rotating at 4°C for 30 min. Subsequently, the resin was washed 3x and the protein eluted with elution buffer (100 mM HEPES, 400 mM imidazole, 100 μM GDP, pH 7.5). Collected fractions were analyzed for purity by SDS-PAGE and dialyzed in a buffer containing 20 mM Tris, 50 mM NaCl, 5 mM EDTA, 2 mM DTT, pH 7.5. GDP•Rac1 was generated by incubating free Rac1 with GDP (10-fold excess) at 30°C for 1 h. Mant-GDP•Rac1 was generated by incubating free Rac1 with methylanthraniloyl-GDP (5-fold excess mant-GDP, Life Technologies) at 30°C for 1 h. Nucleotide exchange was quenched by addition of 250-fold excess of $MgCl_2$ and excess nucleotide was removed by dialysis into assay buffer (20 mM Tris, 50 mM NaCl, 10 mM $MgCl_2$, 1 mM DTT, 1% glycerol, pH 7.5). GTPase loaded with mant-GDP was stored at 4°C and used within 1 week. Rac1 loaded with GDP was aliquoted, snap-frozen and stored at −80°C.

Guanine nucleotide exchange assays

To evaluate inducible nucleotide exchange, 250 nM of a given CIAR construct was incubated with 200 nM MANT-GDP (Life Technologies, M-12414), and 25 μM or 5 μM of free BH3 peptide (APPNLWAAQRYGRELRRMSDEFEGSFK) or NOXA control peptide (PAELEVECATQLRRFGDKLNFRQKLL) in black 96-well plates in triplicate wells. Free peptides were synthesized by GenScript. 10μM HRAS-GDP was added and the change in fluorescence was monitored with a Victor^3 V Multilabel Plate Reader (Perkin Elmer, excitation at 355 nm and emission at 460 nm). Background exchange for HRAS•GDP was also determined in the absence of CIAR constructs. Final reaction volume for each assay well was 125 μL. Triplicate values for each time point were averaged. The rate of fluorescence change—a proxy for MANT-GDP association rate—was determined via linear regression of the linear phase for each assay. For determination of fold change, the following equation was used:

$$\frac{slope\ (BH3) - slope(HRAS\ alone)}{slope\ (control\ BH3) - slope(HRAS\ alone)}.$$

VAV constructs were assayed by mixing the construct of interest (800 nM final concentration), mant-GDP•RAC1 (2 μM final concentration), and excess GDP (400 μM final concentration) in assay buffer (20 mM Tris, 50 mM NaCl, 10 mM $MgCl_2$, 1 mM DTT, 1% glycerol, pH 7.5), and 5 μM competitor or control BH3 peptide. The change in fluorescence was measured using a Victor^3 V Multilabel Plate Reader (Perkin Elmer, excitation at 355 nm and emission at 460 nm). Control experiments were performed that measured the rate of spontaneous nucleotide exchange in the absence of the sVAV construct; mixtures contained mant-GDP•RAC1 (2 μM final concentration) and excess GDP (400 μM final concentration). The final volume of each assay well was 125 μL. All assays were performed in triplicate in 96-well black plates. The rate of fluorescence change—a proxy for MANT-GDP dissociation rate— was determined via linear regression of the linear phase for each assay. For determination of fold change, the following equation was used:

$$\frac{slope\ BH3 - slope(RAC1\ alone)}{slope\ (control\ BH3) - slope(RAC1\ alone)}.$$

Cell culture and stable cell line generation

Flp-In T-Rex 293 cells were maintained in high glucose DMEM, 10% FBS, 4 mM L-glutamine (Life Technologies). MCF10A lines were grown as previously described[54]. Doxycycline-inducible CIAR-293 and xCIAR-293 cells were generated according to manufacturer's instructions. Briefly, Flp-In T-REx 293 cells were transfected with S. 17.3_pcDNA5/FRT/TO (CIAR) or xS.17.3 pcDNA5/FRT/TO (xCIAR), followed by selection with hygromycin for 7–10 days. After induction with 1 μg/mL doxycycline, expression of the desired transgenes was verified via immunoblot. CIAR-293 and xCIAR-293 cells were maintained in the same media as above supplemented with 50 μg/mL hygromycin and 10 μg/mL blasticidin.

Lentiviral expression vectors were packaged and target MCF10A cells (American Type Culture Collection (ATCC)) transduced according to standard protocols[55]. Briefly,

HEK-293T cells were seeded and co-transfected with packaging vectors psPAX2 and pMD2.G, and the indicated pLenti transfer vector. Virus-containing conditioned media was collected 2 days after transfection and clarified using a 0.45 μM filter. Prior to infection, virus-containing media was diluted 1:4 in normal MCF10A growth media and the mix was supplemented with polybrene to a final concentration of 8 μg/mL. Subsequently, the viral transduction mix (5 mL) was added to target MCF10A cells, seeded to 30% confluence, and incubated for 24 hours. Virus-transduced MCF10A cells were given one day to recover and then selected in puromycin for 2 days. Expression of the desired transgenes was verified via immunoblot. Cell lines were confirmed to be free of mycoplasma.

Luciferase-based Serum Response Element (SRE) Assay

Flp-In T-REx 293 cells were plated in 96-well plates and transfected the following day with a given candidate CIAR construct, reporter luciferase plasmid (luc2P), and control luciferase plasmid (Renilla). Transfections were carried out using XTremeGENE-HP according to the manufacturer's instructions (Roche). After 4 h at 37°C, cells were changed to serum free media supplemented with 1 μg/mL doxycycline. 24 h later, cells were changed to serum free media containing either A3 (25 μM or 10 μμ), DMSO, or the MEK inhibitor AZD6244 (40 μM, Selleck Chemicals) and incubated at 37°C. After 6 h, luc2P luciferase and Renilla luciferase activity was quantified using the Dual-Glo™ Assay System (Promega). Data was processed and analyzed as follows: (1) background signal present in non-transfected wells was subtracted from all wells, (2) intra-well normalization was performed by dividing luc2P signal by Renilla signal to control for variation in transfection efficiency, (3) residual signal present in the context of MEK-inhibition by AZD6244 was defined as zero RAS/MAPK activation and subtracted for each transfection. Finally (4), fold induction was calculated by dividing signal after A3 treatment by signal after DMSO treatment. All experiments were performed in triplicate.

Immunoblotting

CIAR-293 or xCIAR-293 cells were plated in 12- or 24-well plates in high glucose DMEM (10% FBS, 4 mM L-glutamine, 1 μg/mL doxycycline). The following day, cells were switched to serum-free media and serum starved overnight—except in Fig 3e, in which cells were not serum starved. Cells were then treated with A3, EGF, or DMSO for the indicated duration. For experiments incorporating vemurafenib, cells were treated with vemurafenib or DMSO for 1 h prior to addition of A3 or DMSO. MCF10A-CIAR cells were plated in 6-well plates in full MCF10A media conditions as previously described[54]. Cells were starved overnight in 950ml serum-free and EGF-free MCF10A media prior to stimulation.

Lysates were collected by placement of the plate onto ice, washed with ice cold DPBS, and lysed in a modified RIPA buffer (50 mM Tris-HCL, pH 7.8, 1% IGEPAL CA-630, 150 mM NaCl, 1mM EDTA, 2 mM Na_3VO_4, 30mM NaF, Pierce Protease Inhibitor Tablet). Cleared lysates were subjected to SDS-PAGE and transferred to nitrocellulose. Blocking and antibody incubation were done in TBS with 0.1% Tween-20 (v/v) and blocking buffer (Odyssey). Primary antibodies were diluted: total ERK (1:4,000; #9107), phoshpho-ERK (1:2,000; #4370), phospho-AKT (pS473, 1:2,000; #4060), phospho-AKT (T303, 1:2,000; #13038), AKT (1:2,000; #2920), phospho-EGFR (Y1068, 1:2,000; #2236), and α-tubulin

(1:20,000; #3873) (all Cell Signaling Technology); RAF1 (1:2,000, BD Transduction Labs #610151). Blots were washed in TBS with 0.1% Tween-20. Antibody binding was detected by using near-infrared-dye-conjugated secondary antibodies and visualized on the LI-COR Odyssey scanner. Blots were quantified via densitometry with Image Studio™ (LI-COR). In cases where quantification across multiple blots was required, a standard was included for intergel normalization. These blots were incubated with the same antibody dilutions in parallel and imaged with identical Odyssey scanner settings.

RAS binding domain pulldown assays

Cells were plated in 10 cm dishes and serum starved as above.

Following treatment with A3 (10 μM), EGF (10 ng/mL), or DMSO (0 min sample), cells were placed on ice at the appropriate time points, washed with ice cold DPBS, and lysed. RAS binding domain (RBD) pulldown assays were performed using the Pan-RAS activation kit (Cell Biolabs) according the manufacturer's instructions. A representative experiment is shown in Fig. 4a, n = 3 (except n = 2 for 0 min and 120 min).

Sample preparation for phosphoproteomic analysis

Cells were plated in 10 cm or 15 cm dishes and serum starved as above. Following A3 or EGF treatment, plates were placed on ice, washed with ice cold DPBS, and lysed in ice cold 8M Urea. Protein concentration was determined by the BCA assay (Pierce). Samples were reduced with 5 mM DTT at 56 °C for 1 hour, then alkylated with 15 mM iodoacetamide for 1 hour at room temperature in the dark. Samples were diluted 4-fold with 100 mM ammonium acetate, pH 8.9, and digested with Sequencing Grade Modified Trypsin (Promega) at a ratio of 1:100 (trypsin to total protein), overnight at room temperature. Following digestion, peptides were desalted and concentrated using Sep-Pak Plus C18 cartridges (Waters) according to the manufacturer's recommendations. Samples were then dried by vacuum centrifugation, lyophilized, and stored at −80 °C until further processing.

Isobaric labeling of peptide samples

Tryptic peptide samples were labeled with 8-plex iTRAQ reagents (AB Sciex). Lyophilized peptides derived from approximately 400 ug of starting material were resuspended in 30 μL of dissolution buffer (0.5 M $N(Et)_3HCO_3$, pH 8.5–9). iTRAQ labels were resuspended in 70 μL of isopropanol and added to the peptide mixture. Samples were incubated at room temperature for 2 hours, combined, and dried overnight by vacuum centrifugation. The following day, samples were desalted and concentrated using Sep-Pak Vac 1cc (50 mg) cartridges (Waters) according to the manufacturer's recommendations. Samples were then dried by vacuum centrifugation, lyophilized, and stored at −80 °C until further processing.

IMAC

Approximately 100 μL of packed Ni beads (Ni-NTA Superflow beads, Qiagen) were washed three times in water and stripped with 100 mM EDTA, pH 8.9, for 30 min. Beads were then washed three times with water and incubated with 100 mM $FeCl_3$ for 30 min. Beads were then washed three times with water and once with 80% acetonitrile (ACN) in 0.1% trifluoroacetic acid (TFA). Lyophilized iTRAQ samples were resuspended in 1.5 mL of 80%

ACN in 0.2% TFA and incubated with prepared beads for 1 hour at room temperature. Beads were then washed three times with 80% ACN in 0.1% TFA, and phosphopeptides were eluted from beads twice with 75 µL of 1.4% ammonia. Samples were then vacuum centrifuged down to approximately 20 µL. 2 µL of 200 mM ammonium formate, pH 10, was added and samples were directly analyzed by mass spectrometry.

Mass spectrometry

Peptide samples were loaded onto a first dimension trap column (Waters Xbridge, C18, 10 um particle size, 100 A pore size, 4 cm packing length 150 µm column inner diameter). Online peptide separation coupled to MS/MS was performed with a 2D-nanoLC system (nanoAcquity UPLC system, Waters) and a Velos-Pro/Orbitrap-Elite hybrid mass spectrometer (ThermoFisher Scientific). Six discrete elutions were performed at 1.5 µL/min with 5 mM ammonium formate, pH 10, using increasing concentrations of ACN (1%, 3%, 6%, 15%, 25% and 44%) and diluted with 6 µL/min 0.1% formic acid (FA) prior to loading onto a second dimension trap column (Dr. Maisch ReproSil-Pur, C18, 5 um particle size, 120 A pore size, 4 cm packing length 150 µM column inner diameter) connected to an analytical column (Orochem Reliasil, C18, 3 µM particle size, 90 A pore size, 20–25 cm packing length 50 µM column inner diameter) with an incorporated electrospray emitter. Peptide separation was achieved using a gradient from 3 to 80% (V/V) of ACN in 0.1% FA over 115 minutes at a flow rate of 200 nL/min. The mass spectrometer was operated in data-dependent mode using a Top 10 method. Full MS scans (m/z 300–2000) were acquired in the Orbitrap analyzer (resolution = 120,000), followed by high energy collision induced dissociation (HCD) MS/MS (fm/z 100–2000, resolution = 15,000) at a normalized collision energy of 35%.

Data Processing and Analysis

MS data files were searched using the COMET algorithm[56] and the output was imported into the Trans-Proteomic Pipeline[57] with the following parameters: variable oxidation of methionine, variable phosphorylation of serine, threonine, or tyrosine, up to 4 variable modifications per peptide, fixed oxidation of cysteine, and fixed iTRAQ labeling of lysines and the N-terminus, two missed cleavages, maximum charge of 7. Peptide false discovery rate (FDR) was set to 2.5%. Peptide quantification based on the iTRAQ labels was determined using the LIBRA software embedded in the Trans-Proteomic Pipeline[58].

For Principal Components Analysis (PCA), abundance data was log transformed and scaled to have unit variance. PCA was performed using the prcomp function in the R Stats package. Hierarchical clustering and heatmap generation of timecourse data (Fig. 3c) was performed in GENE-E software (Broad Institute) using Euclidean distance and complete linkage clustering. Protein interaction network analysis was carried out using the STRING interactions database (http://string-db.org/).

Parallel Reaction Monitoring

Unlabeled phosphopeptides were first enriched by IMAC. Samples were then loaded onto a trap column (Dr. Maisch ReproSil-Pur, C18, 5 µm particle size, 120 A pore size, 4 cm packing length 150 µm column inner diameter) connected to an analytical column (Orochem

Reliasil, C18, 3 um particle size, 90 A pore size, 20–25 cm packing length 50 um column inner diameter) with an incorporated electrospray emitter. Peptide separation was achieved using a gradient from 3 to 80% (V/V) of acetonitrile in 0.1% FA over 60 minutes at a flow rate of 200 nL/min. Parallel Reaction Monitoring (PRM) analyses were performed on a Q-exactive Plus (Thermo). The acquisition method combined 5 sequential PRM events followed by a full scan event. Precursor ions of the peptides were targeted in preliminary experiments without time-scheduling and confirmed precursors were targeted +/− 3 minutes of the observed elution times in the actual experimental runs. PRM events employed an orbitrap resolution of 17,500, a target automatic gain control (AGC) value of 2e5, and maximum fill times of 100 ms. The precursor ion of each targeted peptide was isolated using a 4-m/z window. Fragmentation was performed with a normalized collision energy of 35 eV. The full scan event employed a 200–1750 m/z range, an orbitrap resolution of 70,000, a target AGC value of 1e6, and maximum fill times of 200 ms. Data analysis integration was performed with Skyline software. Each peptide was confirmed using at least 3 transitions and 3 isotopic peaks for each peptide were summed for quantification. Each peptide was normalized to a peptide containing TJP1 S912, which was found to be unresponsive to A3 and EGF in initial analyses.

Statistical Analysis

Statistical tests of immunoblot densitometry were performed in excel using a one-sided two-sample Student's t-test. For phosphoproteomic analysis, phosphopeptides present in all replicates were determined to have significant changes (Fig. 4a) in abundance for a given condition, X, if $\left|\log_2 \frac{abundance\ (X)}{abundance\ (DMSO)}\right| > 0.5$ and p <0.05, where p was calculated with a two-tail heteroscedastic Student's t-Test. KEGG pathway enrichment of the phosphoproteomic timecourse experiment was assessed with the WEB-based GEne SeT AnaLysis Toolkit using a hypergeometric test with Benjamini-Hochberg multiple-test correction[59,60]. The 485 proteins quantified in all three biological replicates served as the reference set.

Supplementary Material

Refer to Web version on PubMed Central for supplementary material.

Acknowledgments

This research was supported by the NIH (R01GM086858 (D.J.M), R01CA126792 (J.D.), and F30CA189793 (J.C.R.)), the National Science Foundation CAREER Award (CHE-0954242), the DOD BRCP (W81XWH-11-1-0130), and HHMI (P-S.H and D.B.).

References

1. Buskirk AR, Liu DR. Creating Small-Molecule-Dependent Switches to Modulate Biological Functions. Chem Biol. 2005; 12:151–161. [PubMed: 15734643]
2. Inoue T, Heo WD, Grimley JS, Wandless TJ, Meyer T. An inducible translocation strategy to rapidly activate and inhibit small GTPase signaling pathways. Nat Meth. 2005; 2:415–418.
3. Zhou XX, Chung HK, Lam AJ, Lin MZ. Optical control of protein activity by fluorescent protein domains. Science. 2012; 338:810–814. [PubMed: 23139335]
4. Karginov AV, Ding F, Kota P, Dokholyan NV, Hahn KM. Engineered allosteric activation of kinases in living cells. Nat Biotechnol. 2010; 28:743–747. [PubMed: 20581846]

5. Wu YI, et al. A genetically encoded photoactivatable Rac controls the motility of living cells. Nature. 2009; 461:104–108. [PubMed: 19693014]
6. Goreshnik I, Maly DJ. A Small Molecule-Regulated Guanine Nucleotide Exchange Factor. J Am Chem Soc. 2010; 132:938–940. [PubMed: 20020680]
7. Toettcher JE, Gong D, Lim WA, Weiner OD. Light-based feedback for controlling intracellular signaling dynamics. Nat Meth. 2011; 8:837–839.
8. Suh BC, Inoue T, Meyer T, Hille B. Rapid Chemically Induced Changes of PtdIns(4,5)P2 Gate KCNQ Ion Channels. Science. 2006; 314:1454–1457. [PubMed: 16990515]
9. Komatsu T, et al. Organelle-specific, rapid induction of molecular activities and membrane tethering. Nat Meth. 2010; 7:206–208.
10. Toettcher JE, Weiner OD, Lim WA. Using Optogenetics to Interrogate the Dynamic Control of Signal Transmission by the Ras/Erk Module. Cell. 2013; 155:1422–1434. [PubMed: 24315106]
11. Ambroggio XI, Kuhlman B. Design of protein conformational switches. Curr Opin Struct Biol. 2006; 16:525–530. [PubMed: 16765587]
12. Karnoub AE, Weinberg RA. Ras oncogenes: split personalities. Nat Rev Mol Cell Biol. 2008; 9:517–531. [PubMed: 18568040]
13. Boriack-Sjodin PA, Margarit SM, Bar-Sagi D, Kuriyan J. The structural basis of the activation of Ras by Sos. Nature. 1998; 394:337–343. [PubMed: 9690470]
14. Shoemaker AR, et al. A small-molecule inhibitor of Bcl-XL potentiates the activity of cytotoxic drugs in vitro and in vivo. Cancer Res. 2006; 66:8731–8739. [PubMed: 16951189]
15. Huang PS, et al. RosettaRemodel: a generalized framework for flexible backbone protein design. PLoS ONE. 2011; 6:e24109. [PubMed: 21909381]
16. Roose JP, Mollenauer M, Ho M, Kurosaki T, Weiss A. Unusual interplay of two types of Ras activators, RasGRP and SOS, establishes sensitive and robust Ras activation in lymphocytes. Mol Cell Biol. 2007; 27:2732–2745. [PubMed: 17283063]
17. Santos SDM, Verveer PJ, Bastiaens PIH. Growth factor-induced MAPK network topology shapes Erk response determining PC-12 cell fate. Nat Cell Biol. 2007; 9:324–330. [PubMed: 17310240]
18. Olsen JV, et al. Global, In Vivo, and Site-Specific Phosphorylation Dynamics in Signaling Networks. Cell. 2006; 127:635–648. [PubMed: 17081983]
19. Tarcic G, et al. EGR1 and the ERK-ERF axis drive mammary cell migration in response to EGF. FASEB J. 2012; 26:1582–1592. [PubMed: 22198386]
20. Dougherty MK, et al. Regulation of Raf-1 by direct feedback phosphorylation. Mol Cell. 2005; 17:215–224. [PubMed: 15664191]
21. Dhillon AS, et al. Cyclic AMP-dependent kinase regulates Raf-1 kinase mainly by phosphorylation of serine 259. Mol Cell Biol. 2002; 22:3237–3246. [PubMed: 11971957]
22. Zimmermann S, Moelling K. Phosphorylation and regulation of Raf by Akt (protein kinase B). Science. 1999; 286:1741–1744. [PubMed: 10576742]
23. Marquette A, Andre J, Bagot M, Bensussan A, Dumaz N. ERK and PDE4 cooperate to induce RAF isoform switching in melanoma. Nat Struct Mol Biol. 2011; 18:584–591. [PubMed: 21478863]
24. McPhillips F, et al. Raf-1 is the predominant Raf isoform that mediates growth factor-stimulated growth in ovarian cancer cells. Carcinogenesis. 2006; 27:729–739. [PubMed: 16332724]
25. Wixler V, Smola U, Schuler M, Rapp U. Differential regulation of Raf isozymes by growth versus differentiation inducing factors in PC12 pheochromocytoma cells. FEBS Letters. 1996; 385:131–137. [PubMed: 8647237]
26. Lavoie H, Therrien M. Regulation of RAF protein kinases in ERK signalling. Nat Rev Mol Cell Biol. 2015; 16:281–298. [PubMed: 25907612]
27. Kubicek M, et al. Dephosphorylation of Ser-259 regulates Raf-1 membrane association. J Biol Chem. 2002; 277:7913–7919. [PubMed: 11756411]
28. Mason CS, et al. Serine and tyrosine phosphorylations cooperate in Raf-1, but not B-Raf activation. EMBO J. 1999; 18:2137–2148. [PubMed: 10205168]
29. Pandit B, et al. Gain-of-function RAF1 mutations cause Noonan and LEOPARD syndromes with hypertrophic cardiomyopathy. Nat Genet. 2007; 39:1007–1012. [PubMed: 17603483]

30. Kolch W. Coordinating ERK/MAPK signalling through scaffolds and inhibitors. Nat Rev Mol Cell Biol. 2005; 6:827–837. [PubMed: 16227978]
31. Bollag G, et al. Clinical efficacy of a RAF inhibitor needs broad target blockade in BRAF-mutant melanoma. Nature. 2010; 467:596–599. [PubMed: 20823850]
32. Sosman JA, et al. Survival in BRAF V600-mutant advanced melanoma treated with vemurafenib. N Engl J Med. 2012; 366:707–714. [PubMed: 22356324]
33. Oberholzer PA, et al. RAS mutations are associated with the development of cutaneous squamous cell tumors in patients treated with RAF inhibitors. J Clin Oncol. 2012; 30:316–321.
34. Poulikakos PI, Zhang C, Bollag G, Shokat KM, Rosen N. RAF inhibitors transactivate RAF dimers and ERK signalling in cells with wild-type BRAF. Nature. 2010; 464:427–430. [PubMed: 20179705]
35. Hatzivassiliou G, et al. RAF inhibitors prime wild-type RAF to activate the MAPK pathway and enhance growth. Nature. 2010; 464:431–435. [PubMed: 20130576]
36. Kosako H, et al. Phosphoproteomics reveals new ERK MAP kinase targets and links ERK to nucleoporin-mediated nuclear transport. Nat Struct Biol. 2009; 16:1026–1035.
37. Vomastek T, et al. Extracellular signal-regulated kinase 2 (ERK2) phosphorylation sites and docking domain on the nuclear pore complex protein Tpr cooperatively regulate ERK2-Tpr interaction. Mol Cell Biol. 2008; 28:6954–6966. [PubMed: 18794356]
38. Marklund U, Brattsand G, Shingler V, Gullberg M. Serine 25 of oncoprotein 18 is a major cytosolic target for the mitogen-activated protein kinase. J Biol Chem. 1993; 268:15039–15047. [PubMed: 8325880]
39. Courcelles M, et al. Phosphoproteome dynamics reveal novel ERK1/2 MAP kinase substrates with broad spectrum of functions. Mol Syst Biol. 2013; 9:669–669. [PubMed: 23712012]
40. Dueber JE, Yeh BJ, Chak K, Lim WA. Reprogramming Control of an Allosteric Signaling Switch Through Modular Recombination. Science. 2003; 301:1904–1908. [PubMed: 14512628]
41. Dueber JE, Mirsky EA, Lim WA. Engineering synthetic signaling proteins with ultrasensitive input/output control. Nat Biotechnol. 2007; 25:660–662. [PubMed: 17515908]
42. Yeh BJ, Rutigliano RJ, Deb A, Bar-Sagi D, Lim WA. Rewiring cellular morphology pathways with synthetic guanine nucleotide exchange factors. Nature. 2007; 447:596–600. [PubMed: 17515921]
43. Bos JL, Rehmann H, Wittinghofer A. GEFs and GAPs: Critical Elements in the Control of Small G Proteins. Cell. 2007; 129:865–877. [PubMed: 17540168]
44. Prior IA, Lewis PD, Mattos C. A Comprehensive Survey of Ras Mutations in Cancer. Cancer Res. 2012; 72:2457–2467. [PubMed: 22589270]
45. Ory S, Zhou M, Conrads TP, Veenstra TD, Morrison DK. Protein Phosphatase 2A Positively Regulates Ras Signaling by Dephosphorylating KSR1 and Raf-1 on Critical 14-3-3 Binding Sites. Current Biology. 2003; 13:1356–1364. [PubMed: 12932319]
46. Zhang BH, et al. Serum- and glucocorticoid-inducible kinase SGK phosphorylates and negatively regulates B-Raf. J Biol Chem. 2001; 276:31620–31626. [PubMed: 11410590]
47. Haling JR, et al. Structure of the BRAF-MEK complex reveals a kinase activity independent role for BRAF in MAPK signaling. Cancer Cell. 2014; 26:402–413. [PubMed: 25155755]
48. McKay MM, Ritt DA, Morrison DK. RAF Inhibitor-Induced KSR1/B-RAF Binding and Its Effects on ERK Cascade Signaling. Current Biology. 2011; 21:563–568. [PubMed: 21458265]
49. Heidorn SJ, et al. Kinase-dead BRAF and oncogenic RAS cooperate to drive tumor progression through CRAF. Cell. 2010; 140:209–221. [PubMed: 20141835]
50. Callahan MK, et al. Paradoxical Activation of T Cells via Augmented ERK Signaling Mediated by a RAF Inhibitor. Cancer Immunol Res. 2014; 2:70–79. [PubMed: 24416731]
51. Huang PS, et al. RosettaRemodel: a generalized framework for flexible backbone protein design. PLoS ONE. 2011; 6:e24109. [PubMed: 21909381]
52. Freedman TS, et al. Differences in flexibility underlie functional differences in the Ras activators son of sevenless and Ras guanine nucleotide releasing factor 1. Structure. 2009; 17:41–53. [PubMed: 19141281]
53. Campeau E, et al. A Versatile Viral System for Expression and Depletion of Proteins in Mammalian Cells. PLoS ONE. 2009; 4:e6529. [PubMed: 19657394]

54. Debnath J, Muthuswamy SK, Brugge JS. Morphogenesis and oncogenesis of MCF-10A mammary epithelial acini grown in three-dimensional basement membrane cultures. Methods. 2003; 30:256–268. [PubMed: 12798140]

55. Tiscornia G, Singer O, Verma IM. Production and purification of lentiviral vectors. Nat Protoc. 2006; 1:241–245. [PubMed: 17406239]

56. Eng JK, Jahan TA, Hoopmann MR. Comet: An open-source MS/MS sequence database search tool. Proteomics. 2013; 13:22–24. [PubMed: 23148064]

57. Deutsch EW, et al. A guided tour of the Trans-Proteomic Pipeline. Proteomics. 2010; 10:1150–1159. [PubMed: 20101611]

58. Pedrioli PGA, et al. Automated identification of SUMOylation sites using mass spectrometry and SUMmOn pattern recognition software. Nat Meth. 2006; 3:533–539.

59. Wang J, Duncan D, Shi Z, Zhang B. WEB-based GEne SeT AnaLysis Toolkit (WebGestalt): update 2013. Nucleic Acids Research. 2013; 41:W77–83. [PubMed: 23703215]

60. Benjamini Y, Hochberg Y. Controlling the false discovery rate: a practical and powerful approach to multiple testing. Journal of the Royal Statistical Society Series B. 1995; 57:289–300.

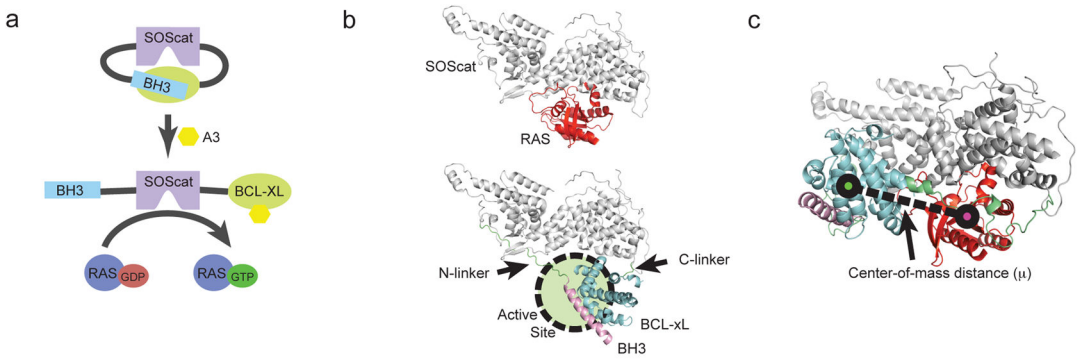

Figure 1. Strategy for engineering a Chemically Inducible Activator of RAS (CIAR)

(a) Schematic depiction of the overall approach for engineering small-molecule controlled autoinhibition of a RAS activator. BCL-xL and a BH3 peptide are appended via flexible linkers to the termini of a constitutively active SOScat mutant (T968L). In the absence of A-385358 ("A3"), a disruptor of the BCL-xL/BH3 interaction, the BCL-xL/BH3 complex occludes the SOScat active site. Upon addition of A3, the BCL-xL/BH3 complex is disrupted and the active site liberated, allowing SOScat to activate RAS. **(b)** Comparison of the structure of SOScat bound to RAS and the desired conformation of CIAR, in which the BCL-xL/BH3 complex occludes the SOScat active site. **(c)** Depiction of μ, the metric used to evaluate output structures from computational modeling of CIAR designs.

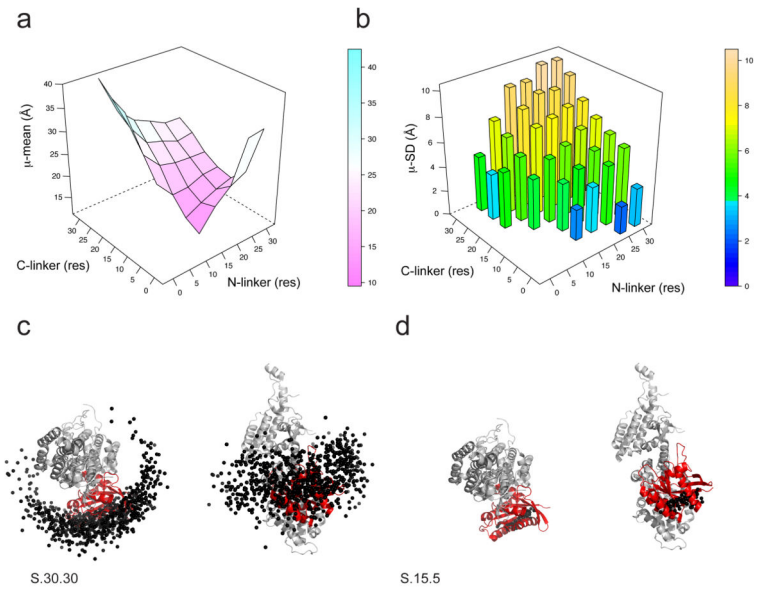

Figure 2. Computational framework for designing CIAR

(a) Average μ (in A) with respect to N- and C-terminal linker length (NL and CL, respectively). **(b)** Standard deviation of μ, as a function of NL and CL. **(c,d)** The BH3/BCL-xL complex mass centers for every trajectory of {NL = 30, CL = 30} **(c)**, and {NL = 15, CL = 5} **(d)**, with BH3/BCL-xL mass centers shown as black spheres, overlaid on the structure of SOScat (cartoon, grey) bound to RAS (red) at its active site. Construct nomenclature: S.(NL).(CL).

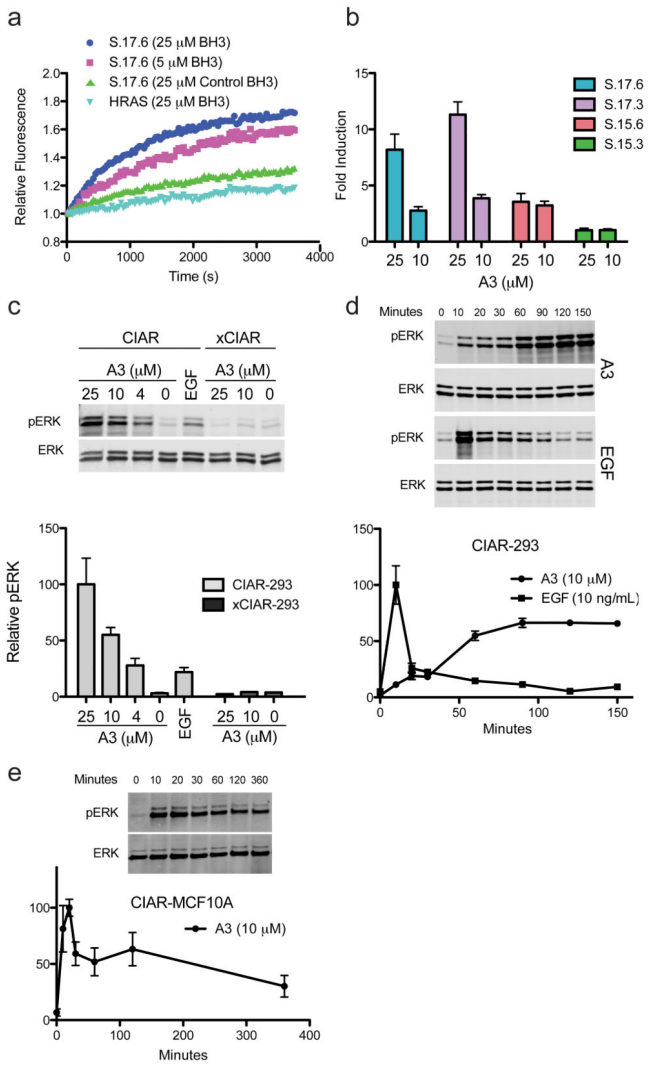

Figure 3. CIAR functions as a RAS rheostat

(a) *In vitro* nucleotide exchange activity on HRAS of a candidate CIAR construct (S.17.6, {NL=17, CL = 6}) in the presence of competitor BH3 or control BH3 peptides. **(b)** Fold induction of the RAS/MAPK pathway in Flp-In T-REx 293 cells relative to DMSO treatment, as measured by a Serum Response Element (SRE) assay. **(c–f)** Phospho-ERK and total ERK immunoblots: **(c)** CIAR-293 and xCIAR-293 cells treated with A3 (4, 10, or 25 μM), EGF (2 ng/mL), or DMSO for 30 minutes. **(d)** Timecourse (0–150 min) of direct RAS activation with A3 (10 μM) or stimulation with EGF (10 ng/mL). **(e)** Timecourse (0–360 min) of direct RAS activation with A3 (10 μM) in CIAR-MCF10A cells. In **(b–e)** error bars = s.e.m (n =3, except in **(e)** n = 4). Uncropped immunoblots available in Supplementary Figs. 18–20.

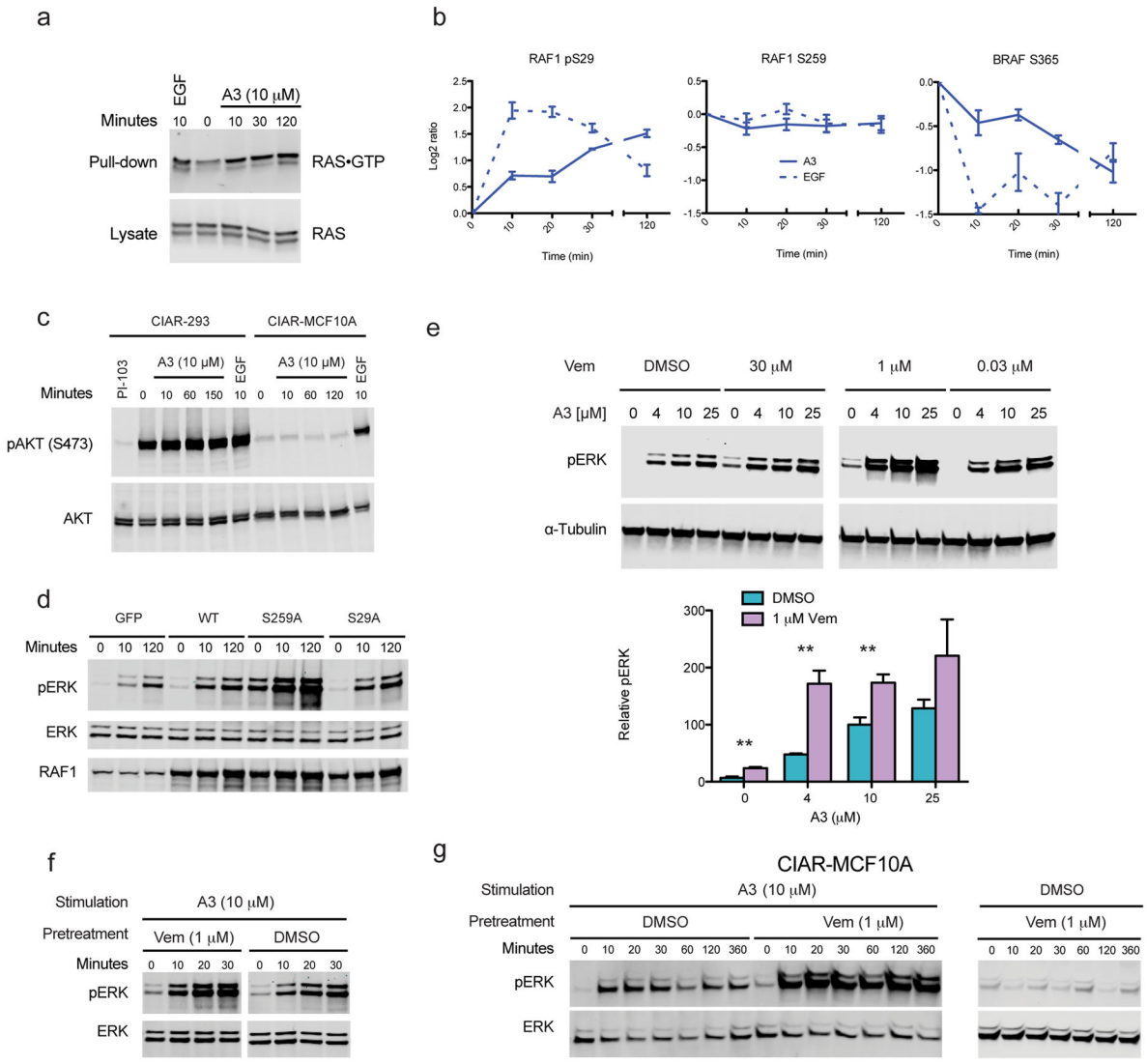

Figure 4. Interrogation of RAF regulation with CIAR

(a) Endogenous RAS•GTP levels after treatment with A3 or EGF (10 ng/mL) for the indicated incubations. **(b)** PRM-MS of three RAF phosphosites in response to direct RAS activation (A3) or EGF stimulation. **(c)** Phospho-AKT and total AKT levels in CIAR-293 and CIAR-MCF10A cells treated with A3, EGF, or PI-103, a pan-PI3K inhibitor. **(d)** CIAR-293 cells were transfected with GFP, wild-type RAF1, or RAF1 containing the indicating mutations. After overnight serum starvation, cells were treated with A3 for the indicated durations. **(e)** CIAR-293 cells incubated with DMSO or varying concentrations of Vemurafenib for 1 h prior to stimulation with varying concentrations of A3 for 30 min. Quantitation of ERK phosphorylation after direct RAS activation of CIAR-293 cells pretreated with DMSO or Vemurafenib (1 μM) (* $p < 0.05$, ** $p < 0.01$). **(f–g)** Timecourse of phospho-ERK and total ERK immunoblot of direct RAS activation in CIAR-293 cells **(f)** and **(g)** CIAR-MCF10As incubated with DMSO or 1 μM Vemurafenib prior to stimulation with A3 (10 μM) for durations indicated. **(b,e)** Error bars = s.e.m, n = 3. **(d–g)**

Representative immunoblots shown, for each n = 3. Uncropped immunoblots available in Supplementary Figs. 21–26.

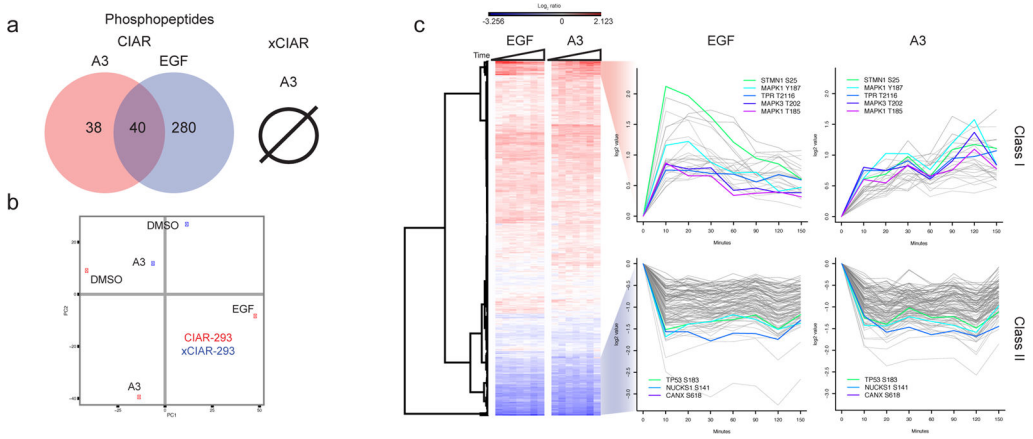

Figure 5. Phosphoproteomic comparison of direct RAS activation and EGF stimulation in CIAR-293 cells

(a–b) CIAR-293 and xCIAR-293 cells were serum starved overnight before direct RAS activation with A3 (10 μM) or stimulation with EGF (10 ng/mL, CIAR-293 cells only) for 30 min (Supplementary Fig. 11a). **(a)** In total, 9,996 phosphopeptides were identified and quantified. Of these, 2,329 phosphopeptides derived from 1,224 proteins were quantified in all biological replicates and used for further analysis. The Venn diagram depicts the number of phosphopeptides showing greater than $|\log_2(0.5)|$ fold-change for each condition relative to treatment with DMSO, with $p < 0.05$. **(b)** Principal components analysis of phosphoproteomic data for CIAR-293 (DMSO, A3 (10 μM), and EGF (10 ng/mL) and xCIAR-293 (DMSO and A3 (10 μM)) samples. **(c)** Timecourse comparison of direct RAS activation and EGF stimulation (Supplementary Fig. 11b.). While 10,767 phosphopeptides were quantified, we analyzed the 657 phosphosites quantified in all replicates at all timepoints for both EGF and A3 treated samples to allow direct in-depth quantitative comparisons. Hierarchical clustering of 657 phosphopeptides present in all replicates reveals two prominent classes (Classes I & II) of peptides with distinct response patterns. Class I and Class II phosphopeptides are plotted with selected peptides highlighted. Mean peptide intensities from triplicate samples were normalized to 0 min intensities then $\log_2$ transformed. Three representative peptides from each class were validated using PRM-MS (Supplementary Fig. 12).

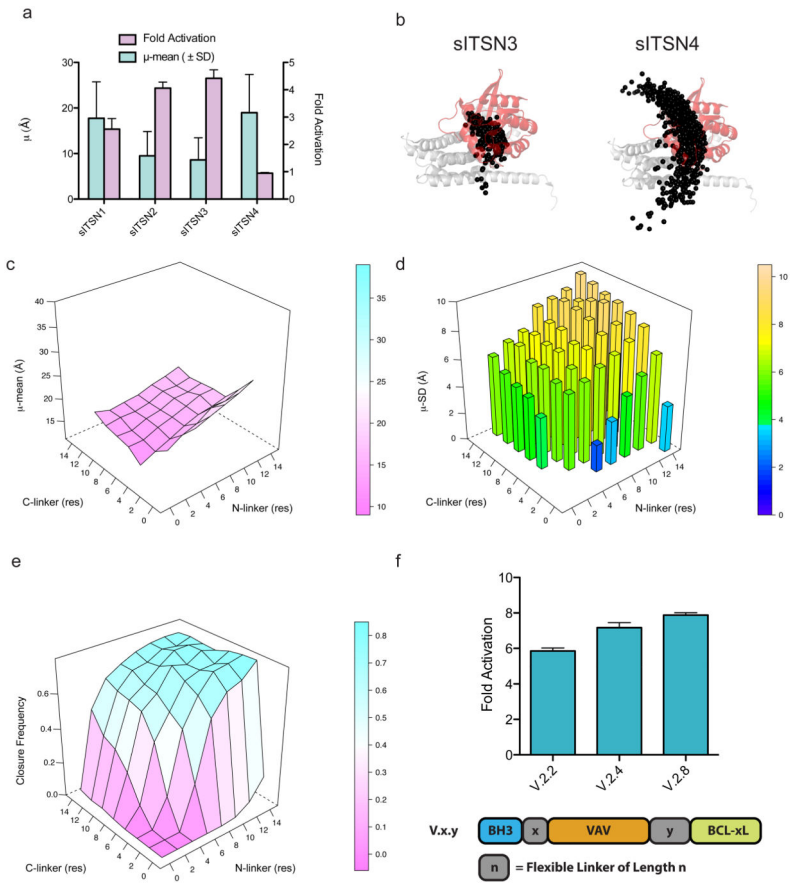

Figure 6. Computational design of inducible Rho Family GEFs

(a–b) Retrospective evaluation of inducible ITSN (sITSN) constructs. **(a)** The relationship of μ and fold-activation of inducible synthetic ITSN (sITSN) designs. **(b)** The BH3/BCL-xL complex mass centers for every trajectory for the indicated designs with BH3/BCL-xL mass centers shown as black spheres, overlaid on the structure of ITSN (cartoon, grey) bound to CDC42 (red) at its active site. **(c–f)** Computational design of an inducible VAV. **(c)** Average μ (in A) with respect to N- and C-terminal linker length (NL and CL, respectively). **(d)** Standard deviation of μ, as a function of NL and CL. **(e)** Closure frequency as a function of NL and CL. **(f)** Fold-activation of inducible VAV constructs. VAV onstruct nomenclature: V.(NL).(CL). **(a,f)** Fold-activation was determined using *in vitro* guanine nucleotide. Constructs were assayed in the presence of 5 μM competitor or 5 μM control BH3 peptides. Fold activation is the ratio of catalytic activity in the presence of a competitor divided by the catalytic activity in the presence of a control. Error bars = s.e.m, n = 3, except for μ-mean in **(a)**.